NUCL SCI TECH (2021) 32:125
https://doi.org/10.1007/s41365-021-00963-2

Effects of impurity elements on SiC grain boundary stability and corrosion

Jun Hui[1] · Bao-Liang Zhang[2] · Tao Liu[1] · Min Liu[1] · Wen-Guan Liu[1]

Received: 16 August 2021 / Revised: 14 September 2021 / Accepted: 3 October 2021 / Published online: 16 November 2021

Abstract Grain boundaries (GBs) have critical influences on the stability and properties of various materials. In this study, first-principles calculations were performed to determine the effects of four metallic impurities (Ni, Al, Bi, and Pb) and three nonmetallic impurities (H, O, and N) on the GBs of silicon carbide (SiC), using the Σ5(210) GBs as models. The GB energy and segregation energy (SE) were calculated to identify the effects of impurities on the GB stability. Electronic interactions considerably influenced the bonding effects of SiC. The formation of weak bonds resulted in the corrosion and embrittlement of GBs. The co-segregation of Bi, Pb, and O was also investigated in detail.

Keywords SiC · First-principles calculation · Grain boundary · Impurity atom · Co-segregation

1 Introduction

Silicon carbide (SiC) [1, 2] exhibits excellent irradiation stability and strength at high temperatures, which has led to its widespread application in reactor core structures, nuclear fuel, and nuclear waste disposal [3, 4]. The aforementioned properties can be primarily attributed to the fact that SiC undergoes oxidation in hot water and high-temperature steam environments, which results in the formation of a protective film of silicon dioxide (SiO_2) [1, 3]. However, the irradiation stability and strength of SiC may decrease in complex and extreme combustion environments. Impurities from the environment or SiC matrix may be enriched along the grain boundaries (GBs) of SiC [4], which leads to GB destabilization and problems such as corrosion, stress concentration, and cracks. In addition, the impurities at SiC GBs contribute to lattice defects that accelerate the corrosion rate of SiC [5]. Irradiation can result in the accumulation of lattice damage and accelerate SiC corrosion [6–8].

The corrosion behaviors of SiC in different environments are complex but are highly influenced by its GBs. Impurity or doping atoms can promote or suppress the intergranular corrosion of SiC. Therefore, the effects of impurities on SiC GBs and the underlying mechanisms of these effects should be investigated. Parish et al. [9] investigated the hydrothermal corrosion behavior of SiC at 603 K and 15 MPa and found that oxide additives, especially Al, were enriched at SiC GBs and induced intergranular corrosion. Doyle et al. [10] revealed that corrosion rarely occurred at the GBs of SiC in an oxygen-free atmosphere. However, in an oxygenated atmosphere, the GBs of SiC were strongly corroded, and fine SiC grains were exfoliated. Ni can improve the GB stability and

This work was supported by the National Natural Science Foundation of China (Nos. 11832019, 11472313, 11572355, and 11705264), the Science and Technology Plan Project of Guangdong Province (No. 2020A0505020005), the Fundamental Research Funds for the Central Universities (No. 19lgpy298), and the State Key Laboratory of Powder Metallurgy, Central South University, Changsha, China.

✉ Wen-Guan Liu
liuwg7@mail.sysu.edu.cn

[1] Sino-French Institute of Nuclear Engineering and Technology, Sun Yat-Sen University, Zhuhai 519082, China

[2] China Institute of Atomic Energy, Beijing 102413, China

corrosion resistance of SiC [11–13]. Under a static corrosion condition [14], SiC exhibits satisfactory corrosion resistance against the coolant of lead-based reactors, namely lead–bismuth eutectic (LBE) [13].

Theoretical simulations have been conducted to study the structural defects and corrosion behavior of SiC [15]. Such simulations can indicate the underlying physical mechanisms of structural defects and corrosive behavior and help overcome the limitations of experimental research (e.g., those limitations related to the irradiation facility, detection limits, and high cost) [15]. Shrader et al. [16, 17] studied the diffusion of Cs, Ag, and B in SiC. By performing first-principles calculations, Zhang et al. [18] determined that the weakening of Si–O and Al–O bonds leads to the accelerated oxidation of SiC. Qing et al. [19] examined the diffusion mechanism of Ag in SiC. However, only a few studies have assessed how impurities affect GB corrosion in SiC. Thus, theoretical simulations are advantageous and essential for investigating the structural defects of SiC.

GBs can serve as channels for rapid diffusion, and impurity or doping atoms can diffuse or cluster at SiC GBs. GBs are considered to be structural defects that are susceptible to corrosion. The vacancies at GBs can capture the atoms introduced through irradiation or doping [20], which may lead to GB embrittlement or corrosion [21–23]. The Σ5 GB is frequently used to investigate the element segregation and corrosion in materials with a face-centered cubic (FCC) structure [24–27]. Rare earth (RE) elements (e.g., Lu, Er, and Ce) have been observed at the GBs of isomeric α-SiC which has an FCC structure [28]. Tan et al. [29] observed Σ5 GBs with a tilt angle of 53° in SiC using electron backscatter diffraction.

In addition to Ni, Pb, and Bi, Al is a doped in SiC ceramics. Moreover, H, N, and O are common and inevitable impurities in SiC. SiC GBs are strongly corroded in oxygenated atmospheres [30–32]. Therefore, Ni, Al, Bi, Pb, H, O, and N were selected as examples in this study to investigate the effects of impurity elements on the stability and corrosion of SiC GBs [33–36]. Moreover, the radii of metallic impurities in SiC are larger than those of nonmetallic impurities in SiC [37–40]; therefore, metallic impurities are usually doped into the GBs of SiC through substitution, whereas nonmetallic impurities are doped into the interstices at the GBs of SiC [41–44].

In summary, in this study, we employed first-principles calculations to examine the effect of metallic impurities (i.e., Ni, Al, Bi, and Pb) and nonmetallic impurities (i.e., H, O, and N) on the GB energy (GBE), segregation energy (SE), co-segregation, and corrosion of the Σ5(210) GBs in SiC. First, we calculated the GBE and SE values of the Σ5(210) GBs with metallic and nonmetallic impurities at various sites. We found that the GBE increased as the atomic radius of the metal impurities increased because the metal atoms could efficiently fill the excess free volume at the Σ5(210) GBs. Second, the effects of temperature and impurity concentration on the GBE were investigated. The GBE varied with the temperature and impurity concentration, and SE was a critical parameter. Third, the bonding mechanism between the impurity atoms and SiC was investigated by analyzing the charge density, density of states, and bond length distribution. Changes in the bond length directly affected the co-segregation of impurities. Finally, impurities that may embrittle the Σ5(210) GBs were identified, and the competing mechanisms influencing the impurity concentrations were analyzed.

2 Computational methods

Two types of impurity segregation are observed at the GBs of SiC: the extra-GB and intra-GB diffusion of impurities. Figure 1a, b illustrate the diffusion of impurities into and along a GB, respectively. As displayed in Fig. 1a, the impurity concentration at a GB increases when the solute atoms can segregate into the GB. After impurities accumulate in the GB plane, interactions occur between them (Fig. 1b). In addition, we considered two situations: the segregation of the same type of impurities (Sects. 3.1and 3.2) and the co-segregation of different types of impurities (Sects. 3.3 and 3.4).

The relaxed lattice constant and Si–C bond length of pure SiC presented in Table 1 are in agreement with those obtained in Fig. 2a displays the model of the SiC bulk supercell used in this study [40–42]. The Σ5(210) GB model and its side view are illustrated in Fig. 2b, c, respectively. Two substitutional sites (*A* and *B*) and one interstitial site (*F*) exist in the GB plane. The vacuum layer of the supercell depicted in Fig. 2a has a thickness of more than 10 Å. As displayed in Fig. 2b, substitutional impurities (Ni, Al, Bi, and Pb) and interstitial impurities (H, O, and N) are doped at the Σ5(210) GBs.

The Vienna Ab initio Simulation Package (VASP) [45] was used to perform electronic state calculations based on density functional theory [46]. Electron–ion interactions were described using the projector-augmented plane-wave method [47]. The total energy was convergent within 10^{-5} eV in the electronic self-consistency steps, and the cutoff energy was 400 eV. The convergent atomic force was 0.01 eV/Å. The atoms in the Σ5(210) GB model were fully relaxed during the structural optimizations; however, the coordinates of the atoms in the outermost layers of the model were fixed. Table 2 presents the atomic electronegativity [48] and corresponding electronic configuration at the VASP potential.

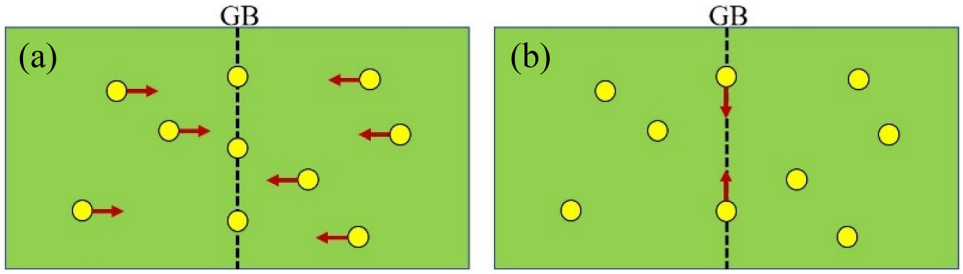

Fig. 1 (Color online) Schematic diagram of impurity diffusion **a** into and **b** along the GB plane

Table 1 Calculated lattice constant and the Si–C bond length (Å) of pure SiC crystal structure, along with the previous results

SiC	Results
Lattice constant	4.371 (This work)
	4.348 [40]
	4.360 [41]
	4.359 [42]
Bond length	1.892 (This work)
	1.851 [41]

3 Results and discussion

3.1 GBE and SE

To identify the effects of impurity or doping atoms on SiC GBs, the stability of these GBs was first determined. The tendency of SiC to form a GB can be characterized by its GBE (γ_{GBE}^{SiC}) [43, 49], which is expressed as follows:

$$\gamma_{GBE}^{SiC} = \frac{E_{GB}^{SiC} - E_{Bulk}^{SiC}}{S}, \quad (1)$$

where E_{Bulk}^{SiC} is the calculated energy of the bulk model in

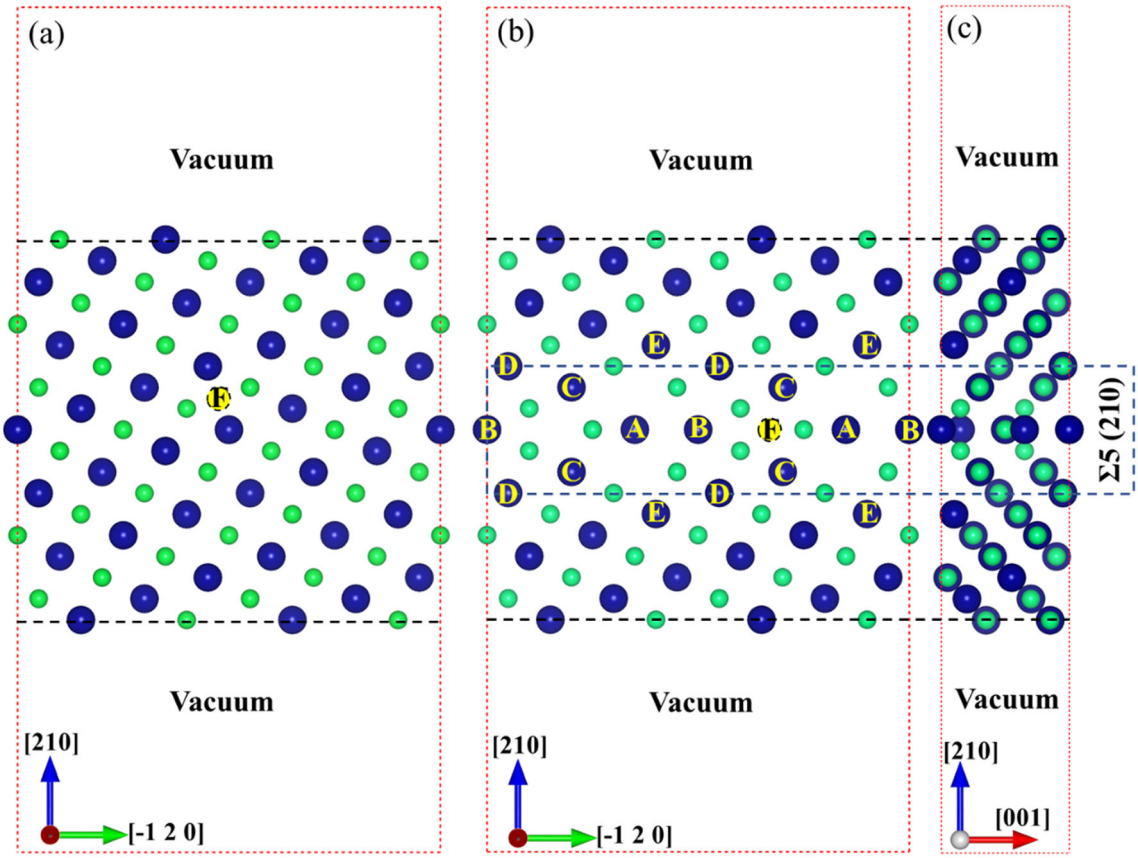

Fig. 2 (Color online) **a** SiC bulk model, **b** SiC Σ5(210) GB model and **c** its side view. *A, B, C, D*, and *E* denote different substitutional sites, and *F* indicates the interstitial site. The bule and green balls represent Si and C atoms, respectively

Table 2 The electronegativity [48] of the elements and their corresponding valence electronic configurations in the VASP potential

Elements	Electronegativity	Electronic configuration
Ni	1.7	$3d^8 4s^2$
Al	1.5	$3s^2 3p^1$
Bi	1.8	$4f^{14} 5d^{10} 6s^2 6p^3$
Pb	1.6	$4f^{14} 5d^{10} 5s^2 6p^3$
Si	1.8	$3s^2 3p^2$
H	2.1	$1s^1$
O	3.5	$2s^2 2p^4$
N	3.0	$2s^2 2p^3$
C	2.5	$2s^2 2p^2$

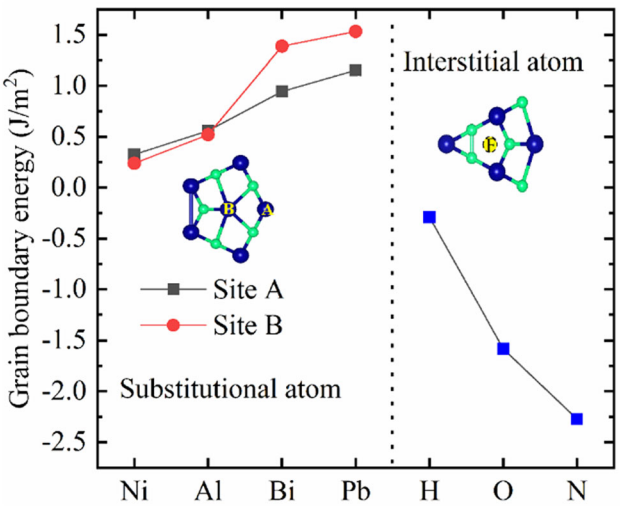

Fig. 3 (Color online) GBEs of impurities at different sites

Fig. 3a, E_{GB}^{SiC} denotes the energy of the GB supercell depicted in Fig. 3b, and S is the GB area. When an impurity *X* is introduced into the SiC GB plane, the corresponding GBE, namely γ_{GBE}^{SiC-X}, can be calculated as follows [43, 49]:

$$\gamma_{GBE}^{SiC-X} = \frac{E_{GB}^{SiC-X} - E_{Bulk}^{SiC-X}}{S} - \gamma_{GBE}^{SiC}, \quad (2)$$

where E_{GB}^{SiC-X} and E_{Bulk}^{SiC-X} represent the total energies of the *X*-doped SiC GB and bulk model displayed in Fig. 3, respectively. The segregation tendencies of impurities at GBs can be indicated by the SE. A negative SE implies that an impurity is prone to segregate into a GB. The SE is defined as follows [49, 50]:

$$E_{SE}^{SiC-X} = \left(E_{GB}^{SiC-X} - E_{GB}^{SiC}\right) - \left(E_{Bulk}^{SiC-X} - E_{Bulk}^{SiC}\right). \quad (3)$$

The GBE of pure SiC was calculated to be 7.57 J/m^2, which is in agreement with the experimental GBE range of approximately 5.5–10.0 J/m^2 [51]. Figure 3 presents the GBEs at the substitutional sites (*A* and *B*), which were doped with metallic impurities, and interstitial site (*F*), which was doped with nonmetallic impurities. According to [43, 49], the higher the GBE is, the more difficult is GB formation. When Si was substituted by Ni, Al, Bi, or Pb, the GBE exhibited a similar trend at sites *A* and *B*. For the metallic impurities, a minimum GBE of 0.23 J/m^2 was obtained for Ni at site *B* and a maximum GBE of 1.53 J/m^2 was obtained for Pb at site *B*. The GBEs for the substitution of Si by H, O, and N (i.e., the nonmetallic impurities) were − 0.28, − 1.58, and − 2.27 J/m^2, respectively, which suggests that these atoms contributed to the formation of the Σ5(210) GBs. Figure 4 displays the correlation between the calculated GBEs and the radii of the impurity atoms. This figure indicates that the GBE is closely correlated with the radius of an impurity atom. A positive linear correlation was observed between the radius of a metallic impurity atom and the GBE, and a negative linear correlation was observed between the radius of a nonmetallic impurity atom and the GBE. Dinda et al. [52] demonstrated the role of atomic size difference between the matrix atom and the doping element in the liquid metal corrosion of steel GBs. They investigated the Sn- and Pb-induced corrosion and embrittlement of steel and found that the Fe–Sn diffusion couple was more susceptible to corrosion caused by doping than was the Fe–Pb diffusion couple. This result was attributed to the relative atomic sizes of Pb and Sn atoms. The results displayed in Fig. 4a are in agreement with the findings of Huang et al. [24, 25].

A negative SE value indicates that the doped atoms are susceptible to segregation at the GBs [53]. The SEs of the different impurity elements at the Σ5(210) GBs are presented in Fig. 5. The SEs of the metal impurities at sites *A*

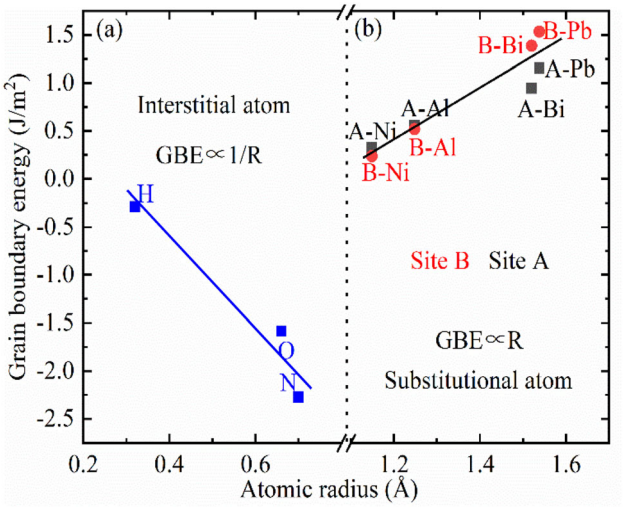

Fig. 4 (Color online) The correlation between the calculated GBE and the radius of impurity elements

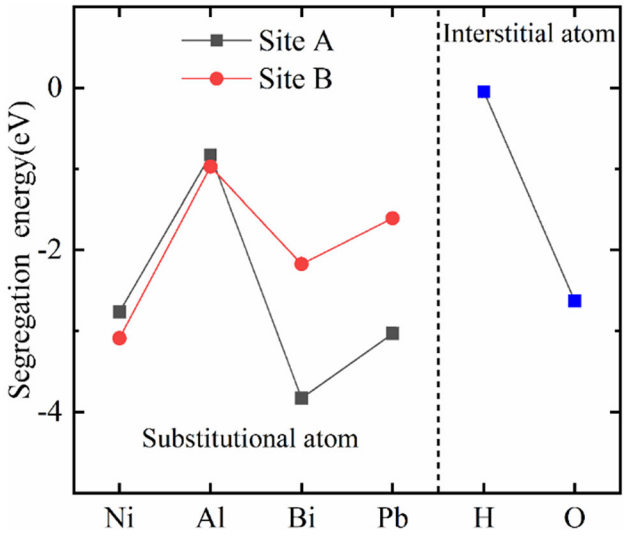

Fig. 5 Calculated SEs of the impurity elements at sites *A*, *B*, and *F*

and *B* were similar and less than 0 eV. For the metal impurities, a minimum SE of − 3.83 eV was obtained for Bi at site *A* and a maximum SE of − 0.83 eV was obtained for Al at site *A*. The SEs of Ni and Al were highly similar, and the SEs of Bi and Pb at site *A* were significantly lower than those at site B. Unfortunately, the N atoms doped into SiC ($E_{\text{Bulk}}^{\text{SiC-N}}$) did not converge at the Σ5(210) GBs. The SEs of O and H were − 2.63 and − 0.04 eV, respectively, which implies that O is easily segregated at the Σ5(210) GBs, whereas H has a high segregation resistance at these GBs.

The SEs for Al and Ni were similar at sites *A* and *B*. Therefore, research must be conducted on why a large difference was observed in the SEs for Bi and Pb. To examine this topic, we calculated the Voronoi volume of the impurity elements. The free volume distortion of the impurity elements was quantified using the Voronoi volume (Table 3) [50]. The radius of an impurity element was proportional to its Voronoi volume (Fig. 6). The Voronoi volume of Si was larger at site *A* than at site *B*. This result indicates that impurity elements with large radii preferentially segregate at site *A*. The aforementioned result is also in agreement with the theory of elastic strain minimization [54]. If an impurity element with a large radius is doped into site *A*, the large Voronoi volume at this site results in a small local strain in the lattice [54]. This conclusion is in agreement with the results of experiments on the segregation of elements such as RE elements and Ag at GBs [55–58].

When impurity elements are introduced at different sites of the SiC Σ5(210) GBs, the temperature- and concentration-induced increments in the GBE can be calculated as follows [43]:

Table 3 Radius [59] and the Voronoi volume of the impurity elements

Impurities	Radius (Å)	Voronoi volumes (Å^3)		
		Substitutional		Interstitial
		Site *A*	Site *B*	Site *F*
Ni	1.149	11.29	12.89	N/A
Si	1.173	10.31	10.04	N/A
Al	1.248	12.41	12.82	N/A
Bi	1.520	14.76	14.62	N/A
Pb	1.538	14.84	14.62	N/A
H	0.320	N/A	N/A	7.560
O	0.660	N/A	N/A	11.61
N	0.700	N/A	N/A	10.66

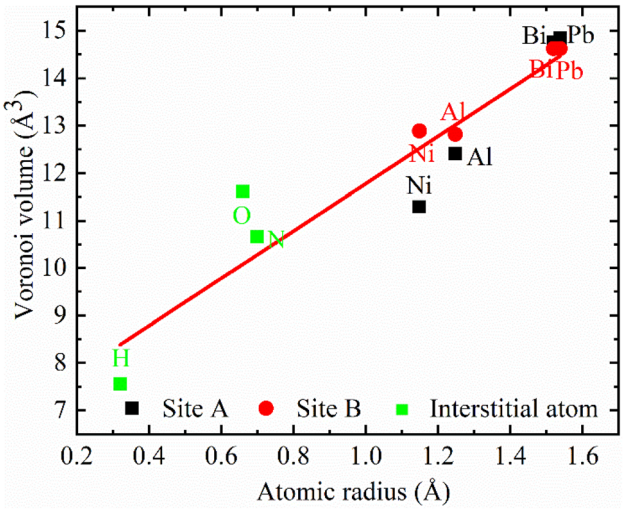

Fig. 6 (Color online) The correlation between the Voronoi volume and the radius of impurity elements

$$\gamma_{\text{GBE}}^{\text{SiC-}X}(K, C_0) = \frac{E_{\text{SE}}}{\left(1 + \exp\left(\frac{E_{\text{SE}}}{\mu K} - \ln\left(\frac{c_0}{1-c_0}\right)\right)\right)S}, \quad (4)$$

where μ, K, and C_0 represent the Boltzmann constant, the temperature, and the concentration of an impurity element, respectively.

We examined the effects of temperature on the GBE. The initial concentration of all the impurity elements in this study was 1.3%. SiC has satisfactory stability at low temperatures and exhibits a phase change at 2000 K [60]. Therefore, the temperature range was set as 1000–2000 K. The GBE of SiC is a function of the temperature (Fig. 7). The SEs of the impurity elements are displayed on the right of the images in Fig. 7. First, the GBEs of Ni, Bi, Pb, and O were positively correlated with the temperature. However, the GBEs of Al and H were not temperature-dependent

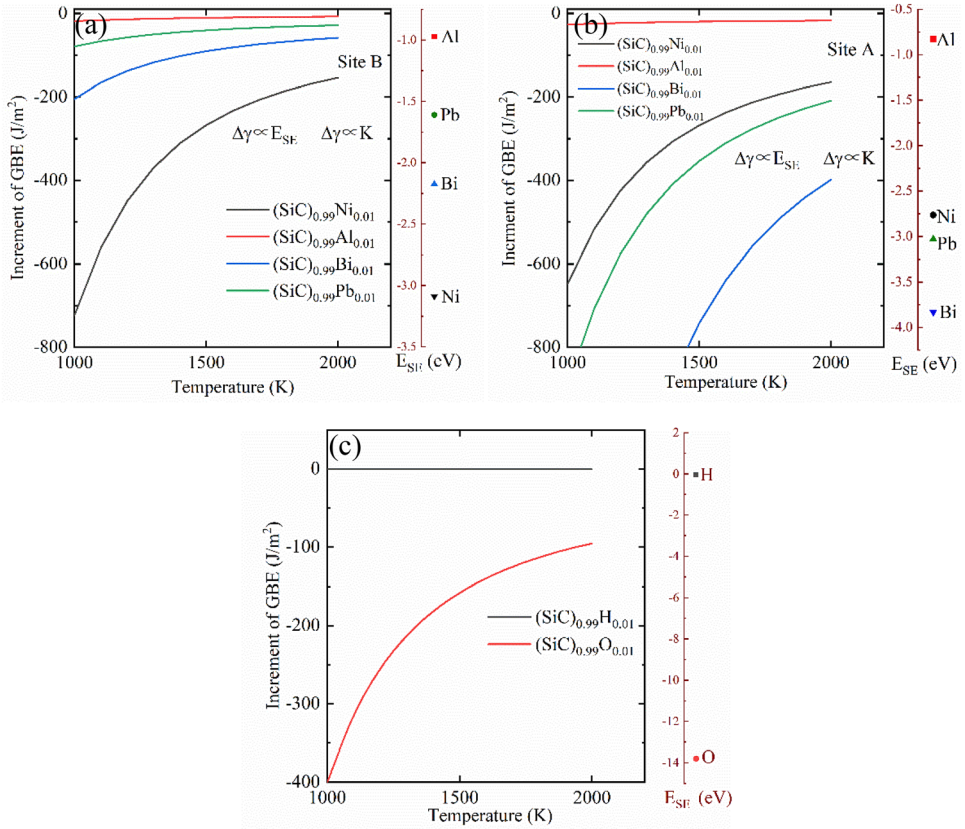

Fig. 7 (Color online) **a**–**c** demonstrate the effects of temperature on GBEs, respectively

because of their large SEs. Second, as illustrated in Fig. 8, the GBEs of the impurity elements were positively correlated with their SEs. Moreover, the GBEs were relatively independent of the temperature when the SEs tended to be positive. Fan et al. [49] found that the GBEs of Y and Sr are positively correlated with their SEs. Shao et al. [61] observed that the GBEs of H doped on stack faults were close to 0 J/m^2 and not temperature-dependent.

The influence of the impurity concentrations on the GBEs was investigated at 1000 K. As displayed in Fig. 8, the GBE decreased with an increase in the concentration of a metal impurity. This result is mainly attributed to the negative SEs of Ni, Al, Bi, and Pb, and a similar phenomenon was noted in our previous Ref. [43, 44]. The GBE of H was not concentration-dependent because of its large SE. Similarly, Shao et al. [61] reported that the GBE of H is not affected by the doping concentration when its SE is close to 0 eV. Fan et al. [49] also found that the GBE (Σ3) is unaffected by the doping concentration when the SE of the doped atoms is close to 0 eV.

According to White–Coghlan theory, the segregation concentration of impurity elements at GBs (C_{GB}) can be calculated as follows [62, 63]:

$$C_{GB} = \frac{1}{1 + \left(\frac{1-C_{bulk}}{C_{bulk}}\right)\exp\left(\frac{E_{SE}^{SiC-X}}{KT}\right)}, \quad (5)$$

where C_{bulk} is the concentration of solute atoms in the bulk. Notably, the entropy term neglected in Eq. (5) may qualitatively modify the temperature dependence of the solute concentration at a GB [64]. This aspect was not considered in the current study.

Figure 9 illustrates the prediction curves for the segregation concentrations of the impurity elements at the Σ5(210) GBs. When the SEs of Ni, Bi, and Pb were negative at 0 K, these impurity elements tended to segregate into the Σ5(210) GBs. As the temperature increased, the segregation concentrations of the aforementioned impurity elements decreased and they were more easily enriched at the substitutional sites without significant segregation. When the SEs of Al and H were only a little negative at 0 K, the segregation resistance of these impurity elements was high at the Σ5(210) GBs. As the temperature increased, the concentrations of the aforementioned impurity elements was consistently close to 0, which indicates that their segregation concentration was saturated at 0 K and that changes in temperature did not increase their segregation concentration.

We employed Eq. (4) to obtain insights into the GBE state at the Σ5(210) GBs. The computed SEs were substituted into Eq. (4); the temperature was set as 1000–2000 K; and the concentrations of the impurity elements were set as 0–10%. Al and H had high SEs, which

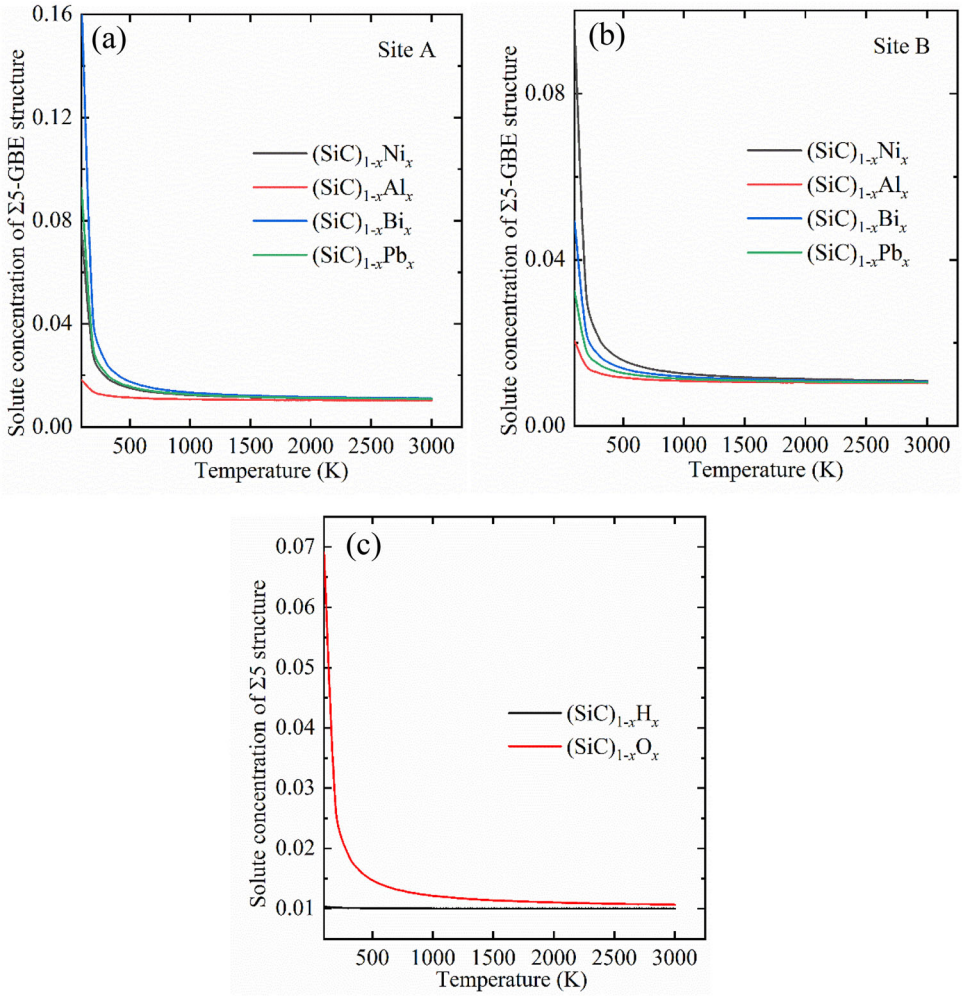

Fig. 8 (Color online) **a**–**c** demonstrate the effects of impurity concentration on GBE, respectively. *x* indicates the impurity concentration in GB

indicates that they exhibited low segregation at the Σ5(210) GBs. The reasons for this result should be explored. Figure 10 displays the GBE of SiC as a function of the temperature and impurity concentration. At site A, the GBE of Al increased from − 573.5 to − 312.5 J/m^2. At site B, the GBE of Al increased from 800.0 to − 450.0 J/m^2. The concentration of Al was positively correlated with the GBE. By contrast, the GBE of H exhibited a low dependence on the temperature. The GBE of Al was lower at site B than at site A, as indicated by the calculated SE values. In addition, the GBE varied between the impurity elements but exhibited only a very weak dependency on the concentration of H. This weak influence of the H concentration on the GBE can be attributed to the weak segregation tendency of H at the Σ5(210) GBs.

3.2 Atomic bonds

To determine the mechanisms of the effects of impurity elements on the GBE, we investigated the charge density and bond length at site *A*. Figure 11 shows the projection of the charge density (from doped to undoped SiC) for the Σ5(210) GBs along the [001] plane. The impurity elements in SiC only affected the local doping location. Accordingly, neither charge redistribution nor charge transfer occurred in the bulk material [63, 65, 66]. C and Si are nonmetallic elements that belong to the IVA group, and C has a stronger ability to obtain electrons than Si does; thus, the electrons lost by the impurity elements were easily obtained by C. As depicted in Fig. 11b–i, the electron clouds of Ni, Al, Bi, and Pb almost did not overlap with that of Si and tended to be close to that of C. As displayed in Fig. 11g, j–l, the electrons lost by H were easily obtained by C. O and N consistently captured the electrons lost by C, which implies that Ni and the interstitial elements preferentially bonded to C. Three doping methods were adopted (Fig. 12): site *A* + H, site *B* + H, and site *A* + site *B* + H. Changes in the impurity site did not affect the preferential bonding tendency of Ni and C.

Figure 13 displays the calculated densities of various SiC states and the doped atoms (Ni, Al, Bi, Pb, H, O, and N) at site *A* of the Σ5(210) GB supercell. As depicted in

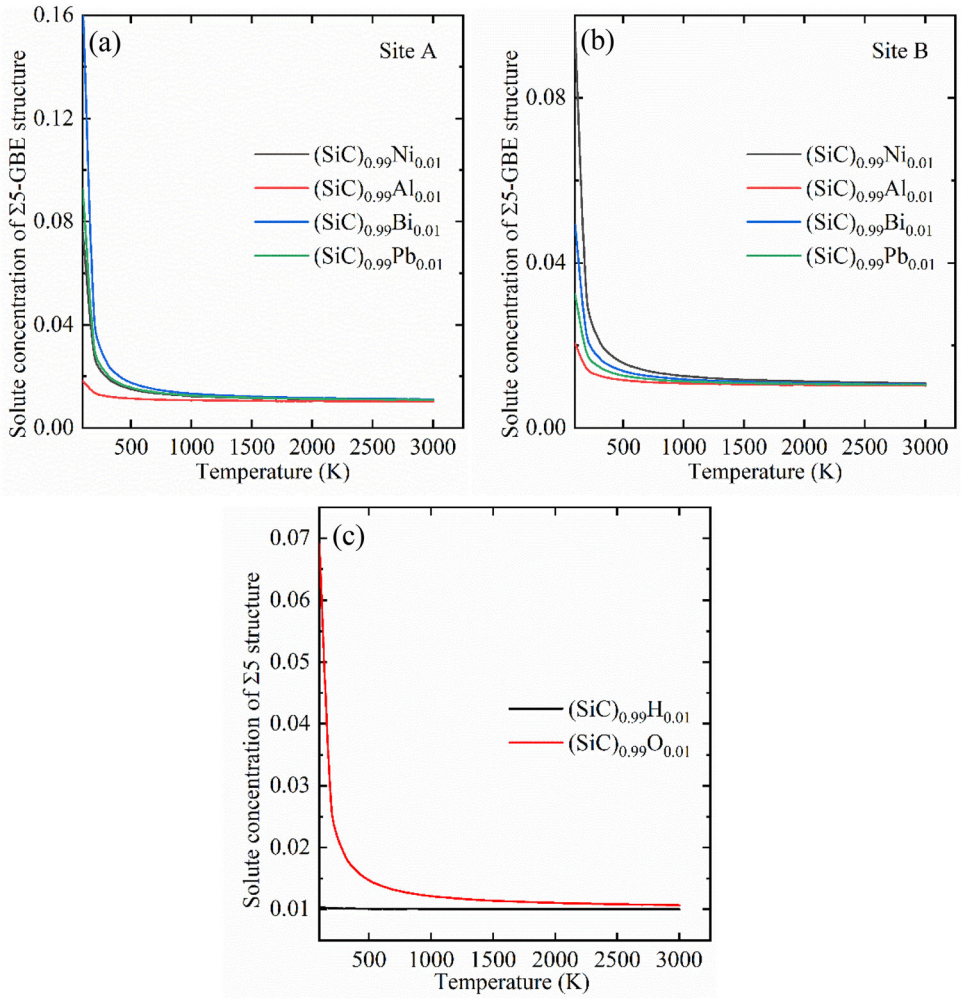

Fig. 9 (Color online) Calculated segregation concentration of impurity elements in the SiC Σ5(210) GB

Fig. 13a, the electron orbitals of Si and C were hybridized. Moreover, the calculated indirect band gap of SiC was 1.90 eV, which was close to the experimental value of approximately 2.20–2.35 eV [67]. As illustrated in Fig. 13d, e, the *p* orbitals of Bi or Pb and C were hybridized, which implies that Bi, Pb, and C formed strong bonds with each other. This result also indicates that SiC has satisfactory corrosion resistance against LBE [13]. The *p*-orbital hybridization of Ni and C/Si (Fig. 13b) may have resulted in the strengthening of SiC GBs. Özkan and Zarghami et al. [11, 12] observed that SiC GBs were strengthened by Ni doping. The peak of Al moved toward the lower-energy region, which resulted in the weakening of the hybridization between Al and C (Fig. 13c). Parish et al. [9] concluded that the enrichment of Al at GBs promotes the intergranular corrosion of SiC. Figure 13g, h illustrate the weak hybridization of O and N with Si/C. The peak of H moved toward the lower-energy region, which weakened the hybridization of H with Si/C (Fig. 13f).

To determine the regularity of the bonding of the impurity elements, the impurities at site *A* were investigated. Figure 14 displays the partial bond lengths at the Σ5(210) GBs with and without the metal impurities. Figure 14f depicts the locations of the different atomic sites. As displayed in Fig. 14, Ni, Al, Bi, and Pb only affected the bond lengths at sites *a*, *b*, and *c*. When impurities were doped at site *A*, the ascending order of the *a*–*A* bond lengths was as follows: 2.397 Å for Ni < 2.488 Å for Bi < 2.505 Å for Pb < 2.510 Å for Al. The maximum *a*–*A* bond length was obtained for pure SiC (2.682 Å); thus, the Ni, Al, Bi, and Pb atoms strengthened the *a*–*A* bonds by reducing the length of these bonds. Ni exhibited the highest bond strengthening effect, and this result is in agreement with the experimental results [11, 12]. The ascending order of the *b*–*A* bond lengths is as follows: 1.877 Å for Ni < 1.938 Å for Al < 2.151 Å for Bi < 2.162 Å for Pb. The lowest *b*–*A* bond length was obtained for pure SiC (1.856 Å); thus, the Al, Bi, and Pb atoms weakened the *b*–*A* bonds by increasing their length. Although the b–A bond length of Ni was marginally longer than that of pure SiC, the difference in their bond lengths was only 0.021 Å. Thus, Ni doping did not lead to a

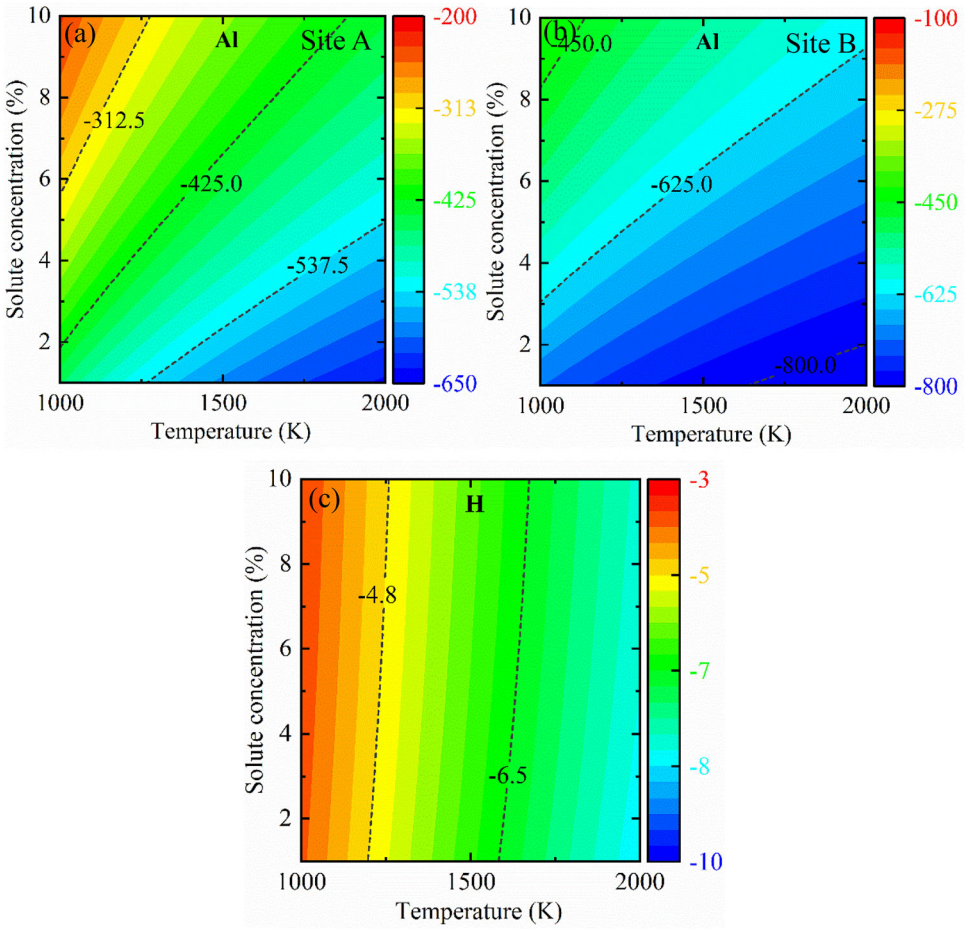

Fig. 10 (Color online) **a**–**c** demonstrate the effects of temperature and concentration on GBEs, respectively

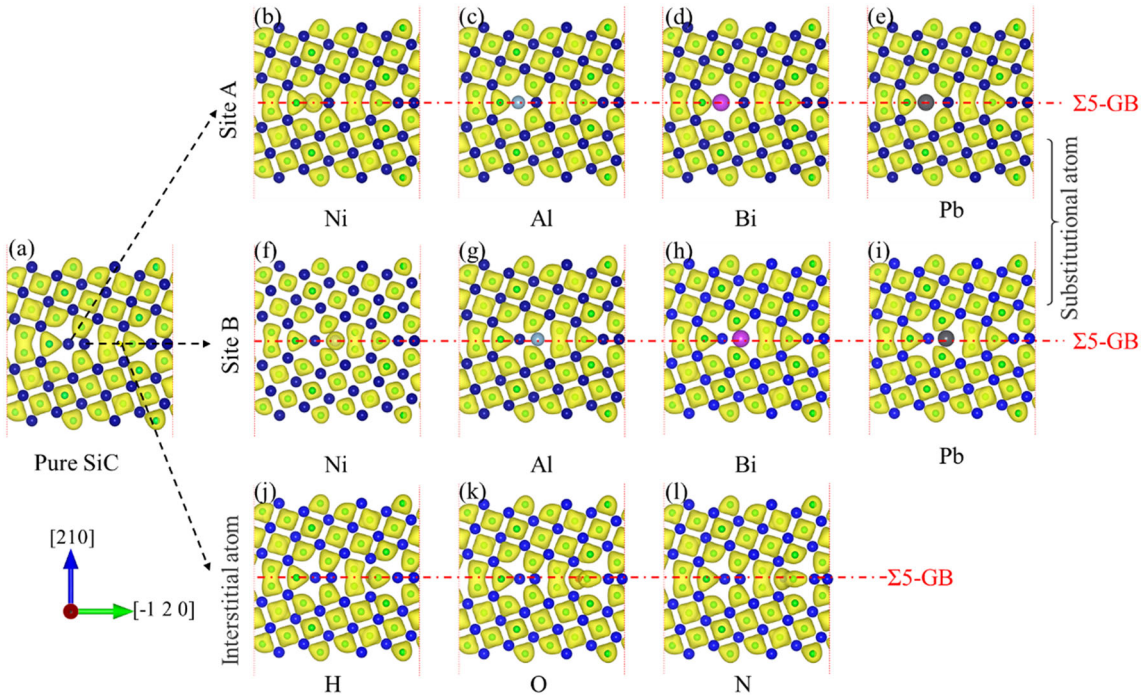

Fig. 11 (Color online) Calculated charge density (e/Bohr^3) of the GB which contains Sites *A* and *B*, and interstitial atom

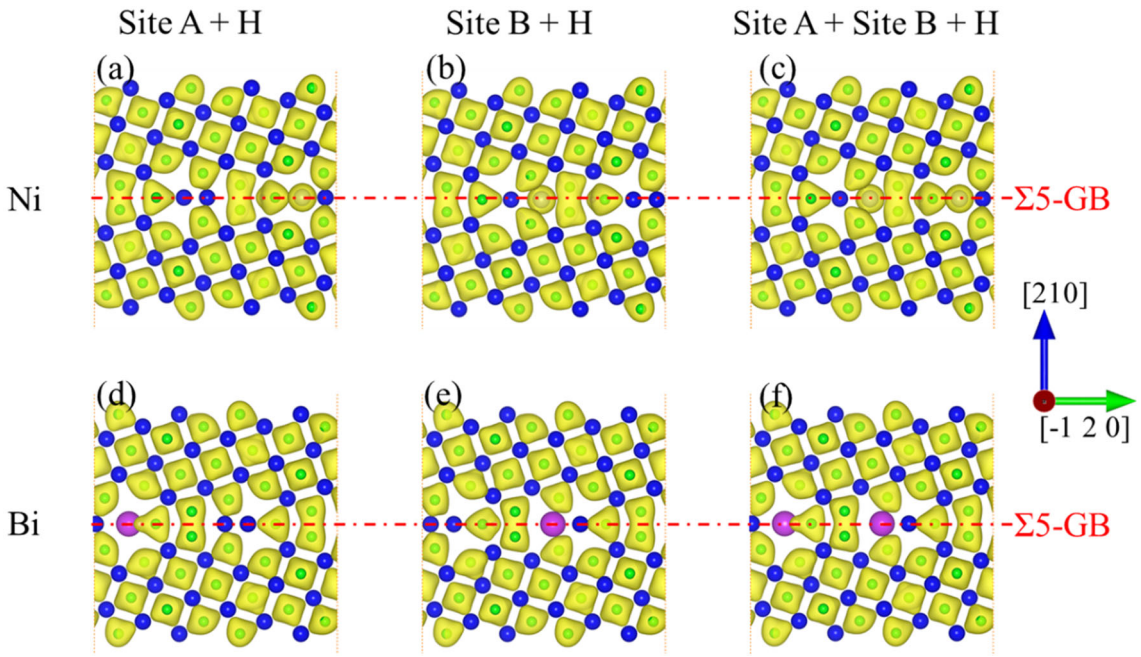

Fig. 12 (Color online) Calculated charge density (e/Bohr^3) of the GB which contains sites A + H, B + H, and A + B + H

significant weakening of the *b–A* bonds. This finding is consistent with the results displayed in Fig. 11a, which indicate that the electron cloud of C has a high overlap with that of Ni.

Figure 15 illustrates the partial bond lengths at the Σ5(210) GBs with and without the nonmetallic impurities. Figure 15e illustrates the locations of the atomic sites. The nonmetallic impurities affected the bond lengths of all the atoms and caused an irregular distribution of bond lengths. Therefore, we only examined the *F–b* and *F–c* bonds of the interstitial impurities. The ascending order of the *F–b* bond lengths is as follows: 1.118 Å for H < 1.303 Å for N < 1.630 Å for O. The ascending order of the *F–c* bond lengths is as follows: 1.602 Å for H < 1.788 Å for O < 1.825 Å for N. One can assume that H may form strong bonds with C and Si and that O may weaken the *F–b* bonds.

3.3 Co-segregation

Figure 5 indicates that Bi, Pb, and O segregation was preferred at the Σ5(210) GBs. Therefore, we investigated the co-segregation of Bi, Pb, and O. To investigate the effects of co-segregation, we calculated the binding energy (BE) as follows [26]:

$$E_{\mathrm{BE}}^{i,j} = \left(E_{\mathrm{GB}}^{\mathrm{SiC}-i} + E_{\mathrm{GB}}^{\mathrm{SiC}-j}\right) - \left(E_{\mathrm{GB}}^{\mathrm{SiC}-i,j} + E_{\mathrm{GB}}^{\mathrm{SiC}}\right), \quad (6)$$

where $E_{\mathrm{GB}}^{\mathrm{SiC}-i,j}$, $E_{\mathrm{GB}}^{\mathrm{SiC}-i}$, and $E_{\mathrm{GB}}^{\mathrm{SiC}-j}$ represent the total energies of the Σ5(210) GBs where some Si atoms were substituted by the atoms of both solutes i and j, solute j only, and solute i only, respectively. A positive BE implied that the interaction between solutes i and j was attractive. The interactions between the atoms at the GBs were mostly weakly attractive; however, some strong repulsive interactions were also noted [68–72].

To investigate the co-segregation of O, Bi, and Pb, the BE was evaluated using Eq. (6). O, Bi, and Pb were doped at the sites where they had the lowest SEs (site *A* for Bi and Pb and site *F* for O; Fig. 16). Table 4 presents the co-segregation of multiple impurities on the Σ5(210) GBs. The BEs of the interactions between Bi and Bi, Bi and Pb, and Pb and Pb were 0.14, 0.13, and 0.11 eV, respectively (i.e., attractive interaction). By contrast, the interaction between O and O was repulsive. According to Scheiber et al. [26], the co-segregation energy of an impurity is equal to the value obtained by subtracting its BE from its SE. If the BE has a high positive value, the SE is low. The interaction of Bi (Pb) with Bi or Pb increased the segregation tendencies of Bi + Bi and Bi + Pb. However, when O was doped at site *F* and Bi or Pb was doped at site *A*, O deviated from its initial position, which resulted in the nonconvergence of the model energy; thus, the BE was a failure.

To analyze the interrelationship among multiple impurities at different temperatures, Scheiber et al. [26, 70] derived the following expression for simultaneously considering multiple sites and solutes [26]:

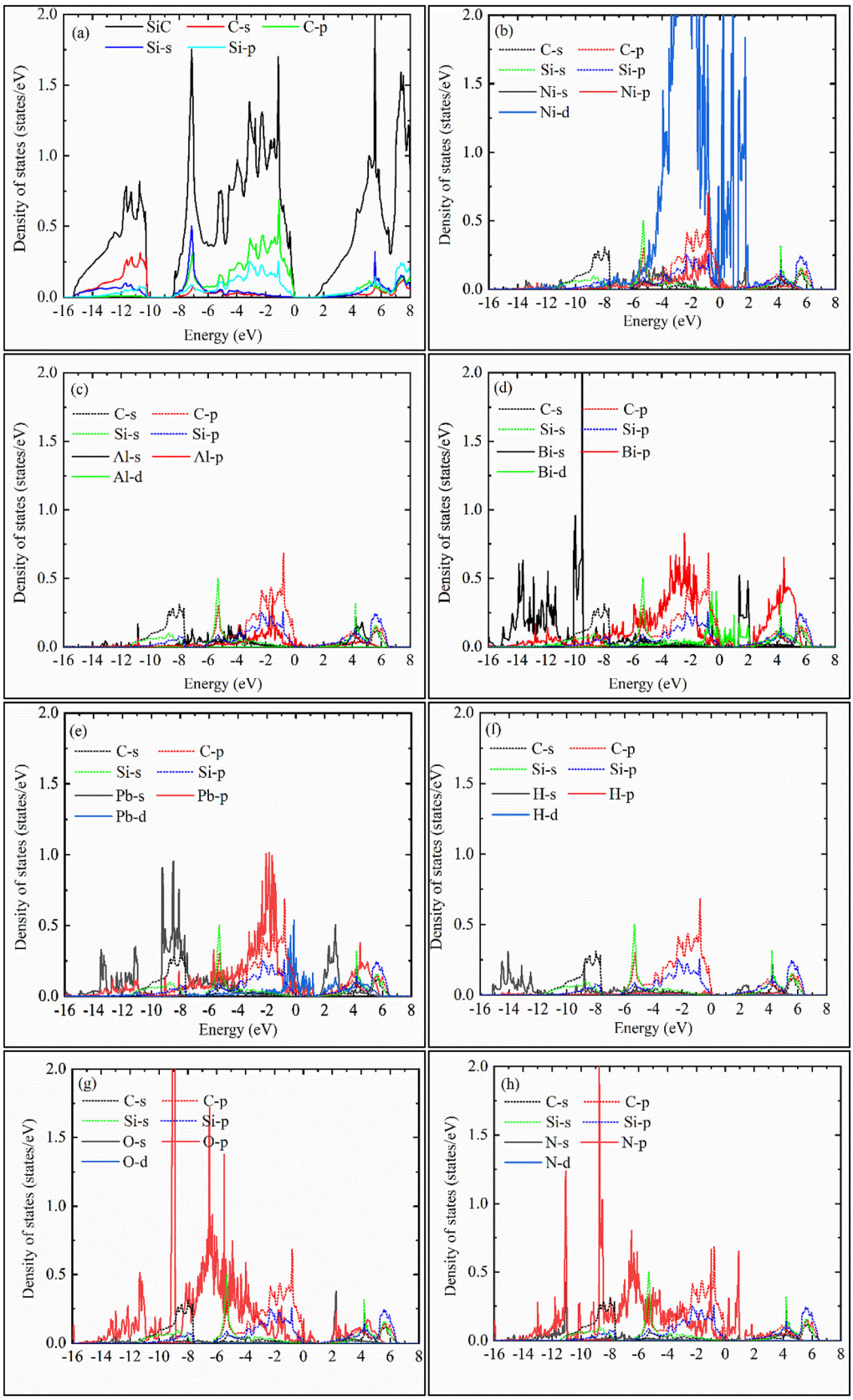

Fig. 13 (Color online) Calculated density of states of SiC, and the impurity elements at site *A* of the GB

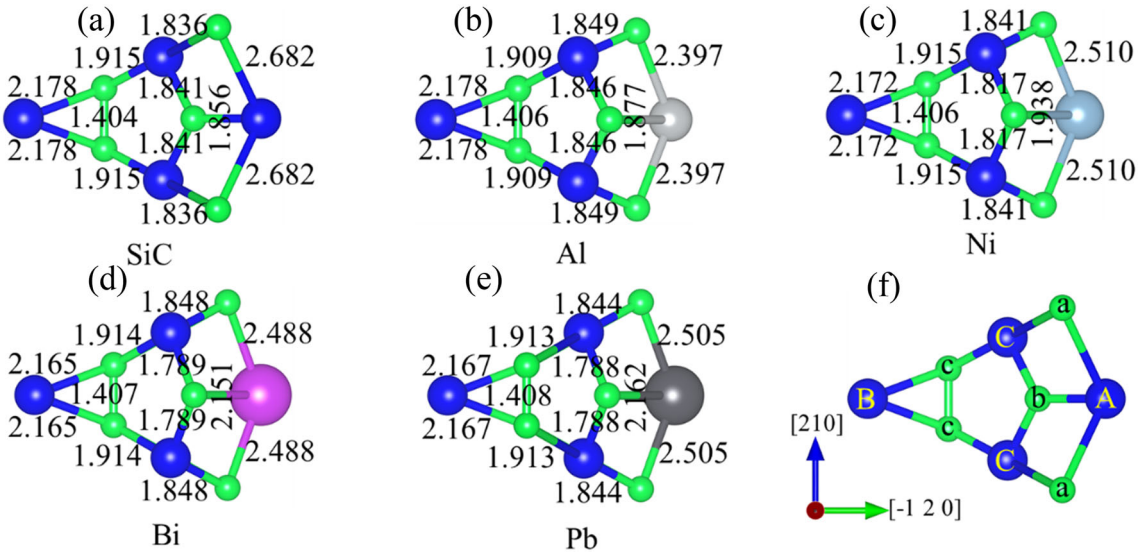

Fig. 14 (Color online) The diagram shows partial bond lengths (Å) on Σ5(210) GB with and without metal impurities. **a** Pure SiC, **b** Ni, **c** Al, **d** Bi, **e** Pb, **f** Numbering of atomic sites

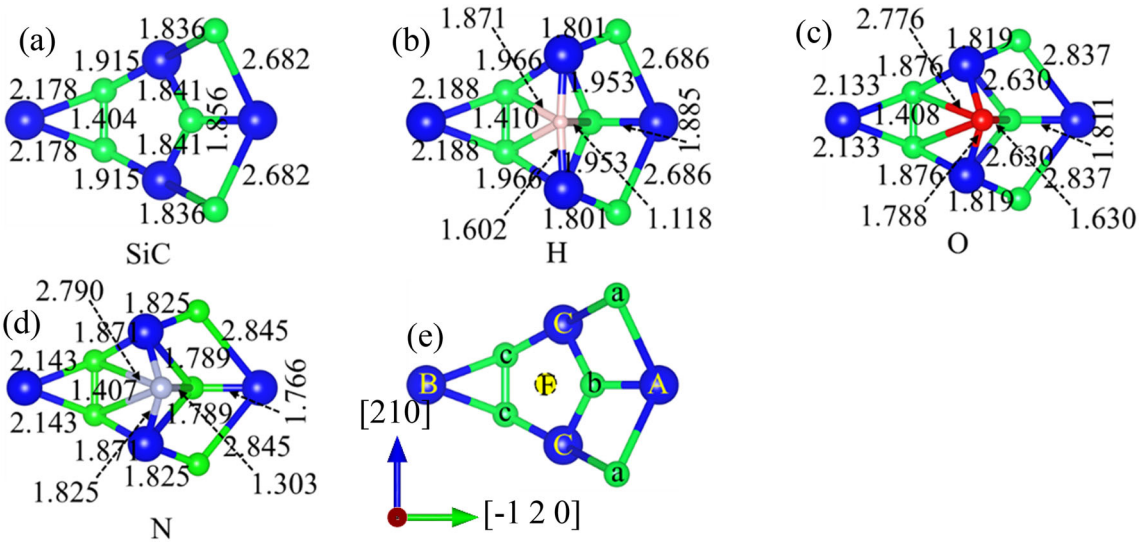

Fig. 15 (Color online) The diagram shows partial bond lengths (Å) on Σ5(210) GB with and without nonmetallic impurities. **a** Pure SiC, **b** H, **c** O, **d** N, **e** Numbering of atomic sites

$$C_{i,\alpha}^{\mathrm{GB}} = \frac{C_i \exp\left(-\frac{E_{\mathrm{SE}}^{i,\alpha}}{KT}\right)}{1 + \Sigma_j C_j \left(\exp\left(-\frac{E_{\mathrm{SE}}^{j,\alpha}}{KT}\right) - 1\right)}, \tag{7}$$

where α denotes the site and C_i denotes the bulk concentration of impurity i.

Using Eq. (7), we determined the relationships among the concentrations of Pb, Bi, and O at temperatures of 500, 1000, 1500, and 2000 K (Fig. 17). The concentrations of Pb and Bi at the Σ5(210) GBs were functions of each other. As depicted in Fig. 17a, when the concentration of Bi was close to 0.5, the concentration of Pb was 0. Thus, the concentrations of Pb and Bi exhibited a negative correlation at the Σ5(210) GBs. As displayed in Fig. 17b, the concentration of Bi reduced to a minimum value and was close to 0 when the concentration of Pb approached 0.5. Figure 17c, d indicate the effect of the O concentration on the Bi and Pb concentrations, respectively. An increase in the O concentration strengthened the repulsive effects of O on Bi and Pb. However, when the concentrations of the aforementioned three impurities were close to 0.1, the repulsion was reduced and perfect co-segregation was achieved. Thus, when the concentrations of the aforementioned impurities were low and close to 0.1, these impurities were attracted to each other and could coexist.

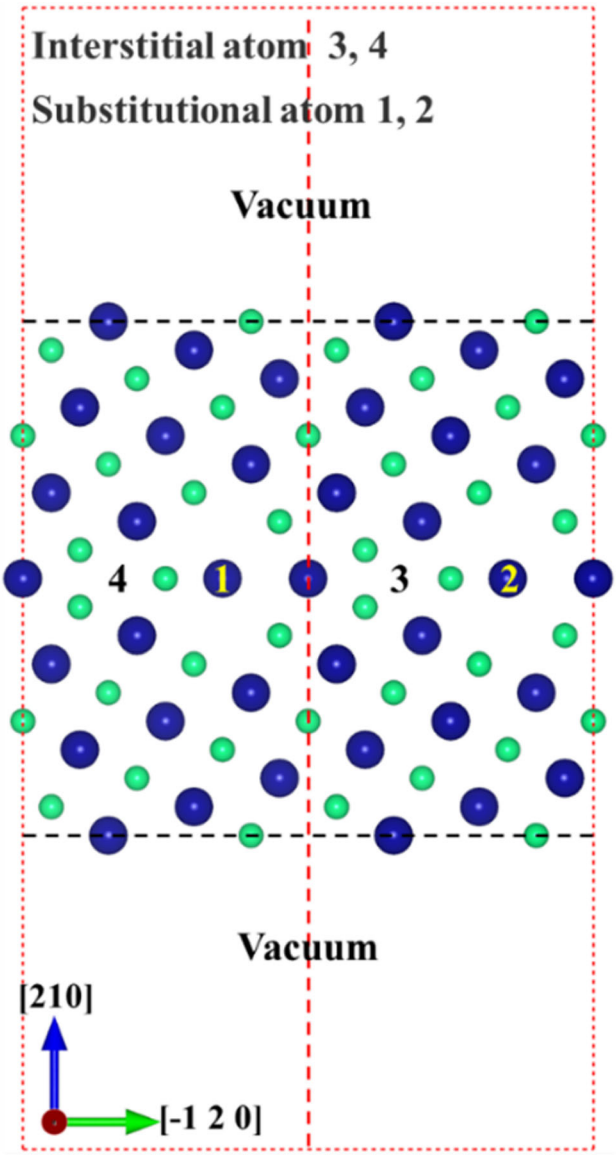

Fig. 16 (Color online) Strongly segregated Σ5(210) GBs with sequence of segregation given by numbers (site 1, 2 for Bi, Pb, site 3, 4 for O)

Table 4 Binding energy of Bi, Pb and O placed at its segregation sites of preferred

Impurities	Binding energy (eV)
Bi + Bi	0.14
Pb + Pb	0.11
Bi + Pb	0.13
O + O	− 2.23
O + Bi	–
O + Pb	–

We employed Eq. (3) to obtain insight into the perfect co-segregation state of multiple impurities at the Σ5(210) GBs. The computed SEs were substituted into Eq. (3). Figure 18 displays the variations in the O concentration with the Bi and Pb concentrations. At 500 K, the O concentration decreased from 0.63 to 0.19% as the Bi and Pb concentrations increased. At 1000, 1500, and 2000 K, the O concentration gradually decreased with increasing Bi and Pb concentrations. The O concentration gradually increased with an increase in the temperature but was negatively correlated with the Bi and Pb concentrations. High Bi and Pb concentrations resulted in the consumption of O at the Σ5(210) GBs, whereas low Bi and Pb concentrations resulted in the enrichment of O at the Σ5(210) GBs. An increase in temperature inhibited the consumption of O by Bi and Pb.

We considered the impurity concentrations of SiC bulk and Σ5(210) GBs to be equal, and the concentrations of impurities at different temperatures were calculated using Eq. (5). To quantify the effect of an impurity i (Bi or Pb) on O enrichment, we introduce the replacement potency λ as the reduction of O at the Σ5(210) GBs if 5% of impurity i is added at the Σ5(210) GBs [26].

$$\lambda(T,\ \mathrm{O}\ : i) = C^{\mathrm{O}}_{\mathrm{GB}}\left(T, C^{i}_{\mathrm{GB}} = 0\right) - C^{\mathrm{O}}_{\mathrm{GB}}\left(T, C^{i}_{\mathrm{GB}} = 5\%\ \right) \tag{8}$$

For impurities that exhibit weak competition with O, λ has a value close to 0, whereas for impurities that do not compete with O, λ has a value of less than 0.

As displayed in Fig. 19a, the highest λ value, which was close to 0, was obtained when the temperature was lower than 500 K, which indicates that the competition between Bi and O was weak. This result is consistent with the results shown in Fig. 18a. When the temperature was increased, λ became less than 0, which indicates that Bi did not compete with O; thus, the consumption of O by Bi and Pb was weak at high temperatures. This result is consistent with the results displayed in Fig. 18b, d. Bi and Pb had similar effects on the O concentration; therefore, the curves displayed in Fig. 19a, b are similar.

3.4 Bonding of co-segregation impurities

According to the doping principle depicted in Fig. 16, Bi or Pb was doped at site A and O was doped at site F. The following pairs of doped atoms were present at the Σ5(210) GBs: Bi + Bi, Pb + Pb, Bi + Pb, and O + O. Unfortunately, when O was doped at site F and Bi or Pb was doped at site A, O deviated from its initial position, which resulted in the nonconvergence of the model energy; thus, the charge density was a failure.

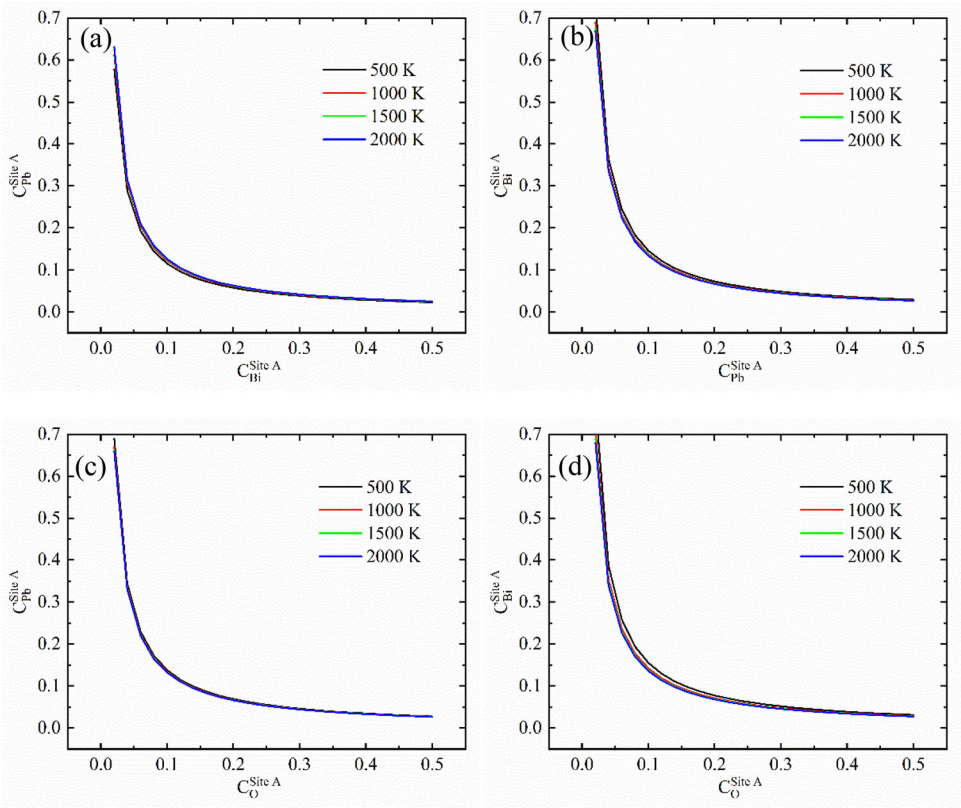

Fig.17 (Color online) Competing relationships between the concentrations of impurities

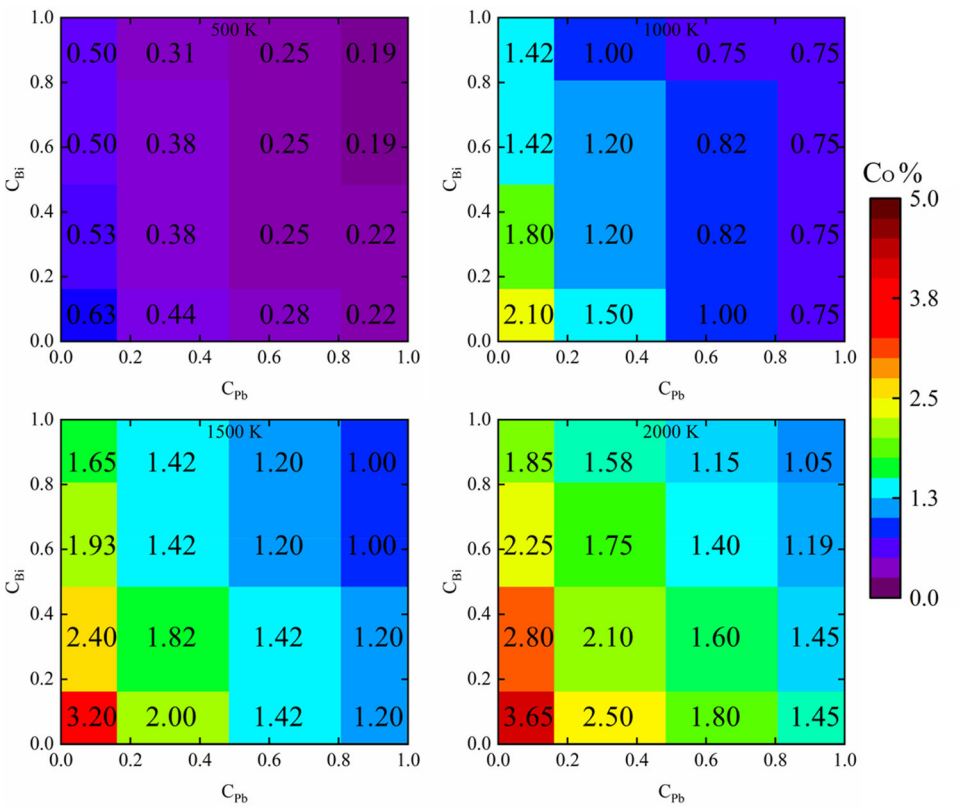

Fig. 18 (Color online) Competing relationships between the concentrations of Bi, Pb and O

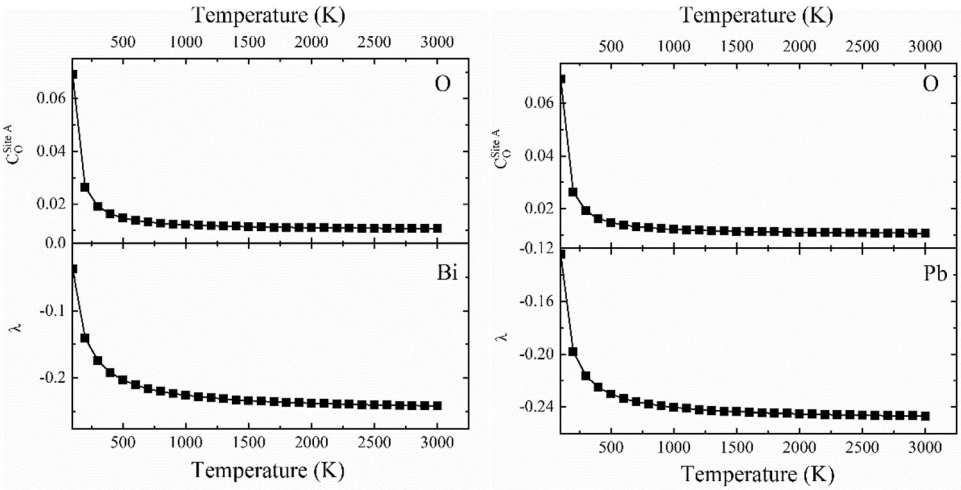

Fig. 19 The O replacement potency of Bi and Pb for different temperatures

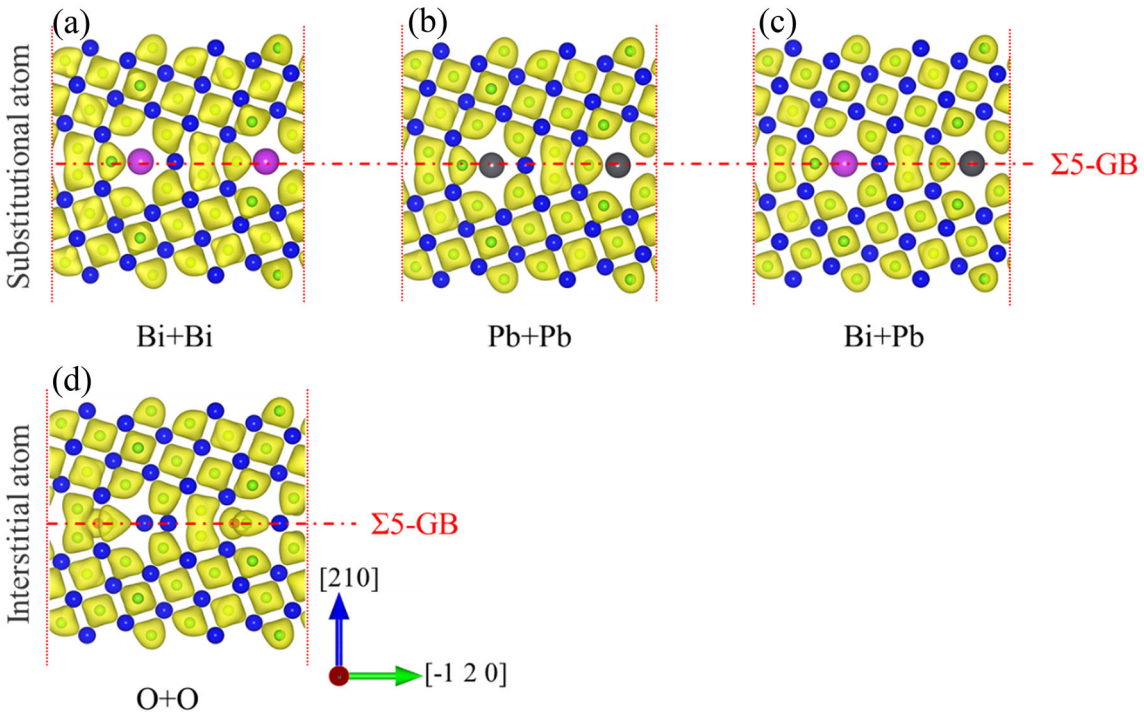

Fig. 20 (Color online) Calculated charge density (e/Bohr^3) of the GB which contains substitutional and interstitial atoms

Figure 20 shows the charge densities of Bi + Bi, Pb + Pb, and Bi + Pb at the Σ5(210) GBs along the [001] plane. The electron clouds of Bi and Pb exhibited a tendency to be close to the electron cloud of C only. This tendency is similar to the electron cloud distribution of Bi and Pb in Fig. 11, which indicates that no strong interactions existed between the metal impurities co-doped at the Σ5(210) GBs. Figure 20d indicates that the O atom on the left side was bonded to three C atoms and that the O atom on the right side was bonded to one C atom. A careful observation of the bonding of these O atoms indicated that they repelled each other. This phenomenon can be quantified by the bond length.

Figure 21 depicts the partial bond lengths at the Σ5(210) GBs with and without the metal impurities. Figure 21e displays the locations of the atomic sites (i.e., sites *A*, *B*, *C*, *a*, *b*, and *c*). Bi + Bi, Pb + Pb, and Bi + Pb only affected the bond lengths of the atoms at sites *a*, *b*, *d* and *B*. When impurities were doped at site *A*, the ascending order of the *a*–*A* bond lengths was as follows: 2.486 Å for Bi

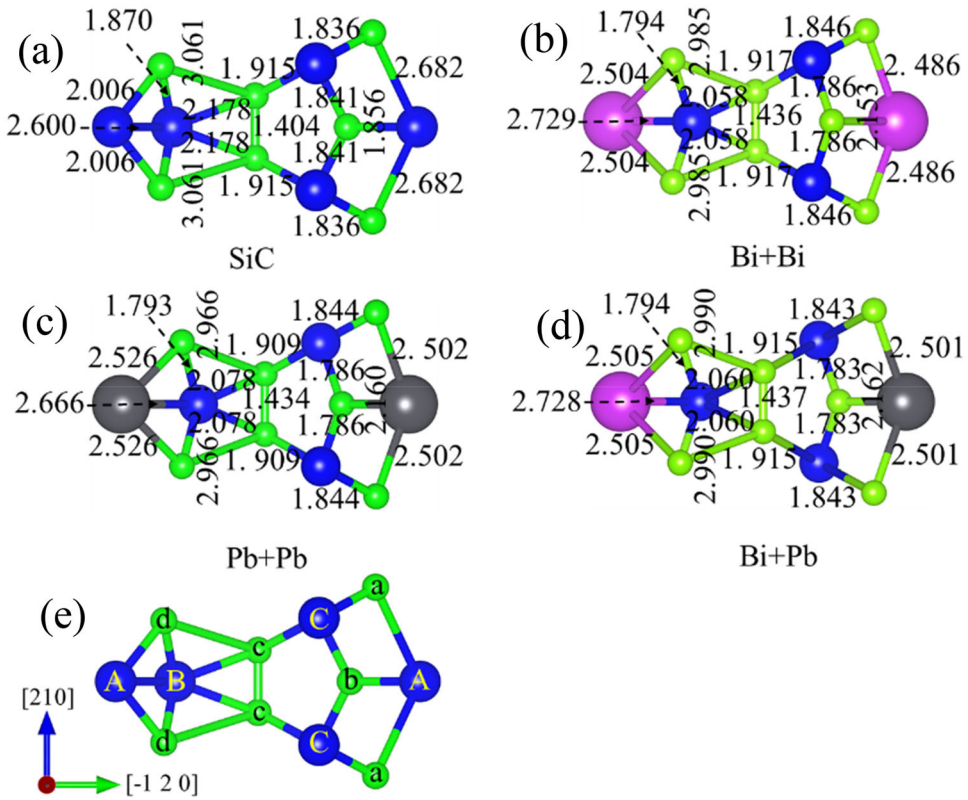

Fig. 21 (Color online) The diagram shows partial bond lengths (Å) on Σ5(210) GB with and without metal impurities. **a** Pure SiC, **b** Bi + Bi, **c** Pb + Pb, **d** Bi + Pb, **e** Numbering of atomic sites

(Fig. 21b) < 2.501 Å for Pb (Fig. 21d) < 2.502 Å for Pb (Fig. 21c). The maximum *a–A* bond length was obtained for pure SiC (2.682 Å); thus, the Bi and Pb atoms strengthened the *a–A* bonds by reducing the length of these bonds. The ascending order of the *b–A* bond lengths is as follows: 2.153 Å for Bi (Fig. 21b) < 2.162 Å for Pb (Fig. 21d) < 2.160 Å for Pb (Fig. 21c). The minimum *b–A* bond length was obtained for pure SiC (1.856 Å); thus, the Bi and Pb atoms weakened the *b–A* bonds by increasing the length of these bonds. The *a–A* and *b–A* bond lengths of Bi and Pb displayed in Figs. 14 and 21 are approximately equal. The *a–A* and *b–A* bond lengths displayed in Fig. 21c, d are also approximately equal. Thus, the bonding of Pb or Bi was not strongly influenced by the other impurities at the Σ5(210) GBs. The ascending order of the *A–B* bond lengths is as follows: 2.666 Å for Pb (Fig. 21c) < 2.728 Å for Bi (Fig. 21d) < 2.729 Å for Bi (Fig. 21b). The minimum *A–B* bond length was obtained for pure SiC (2.600 Å). The ascending order of the *d–A* bond lengths is as follows: 2.504 Å for Bi (Fig. 21b) < 2.505 Å for Bi (Fig. 21d) < 2.526 Å for Pb (Fig. 21c). The minimum *d–A* bond length was obtained for pure SiC (2.006 Å). The aforementioned results indicate that the Bi and Pb atoms weakened the *A–B* and *d–A* bonds by increasing the lengths of these bonds. The *A–B* and *d–A* bond lengths displayed in Fig. 21b, d are approximately equal.

Figure 22 illustrates the partial bond lengths at the Σ5(210) GBs with and without the nonmetallic impurities. Figure 22c displays the locations of the atomic sites. The nonmetallic impurities affected the bond lengths of all the atoms, which resulted in an irregular distribution of bond lengths. In Fig. 22b, the *c–F* bond length is smaller on the left than on the right. This phenomenon is consistent with the charge density distribution of O displayed in Fig. 20d and the mutual repulsion of O + O (Table 4).

4 Conclusion

First-principles calculations were employed in this study to determine the GBEs and SEs at the Σ5(210) GBs of FCC SiC. Four metallic impurities and three nonmetallic impurities were doped at two substitutional (sites *A* and *B*) and one interstitial site (site *F*) at the Σ5(210) GBs of SiC.

First, the GBE had a positive and negative linear correlation with the radius of a metallic and nonmetallic impurity, respectively. The atoms with large radii (Bi and Pb) preferentially aggregated at site *A*. The impurities that formed strong bonds with C were Ni, H, O, and N, and the lengths of these bonds varied.

Second, electronic interactions played a dominant role in the bonding effects. The charge and state densities of the

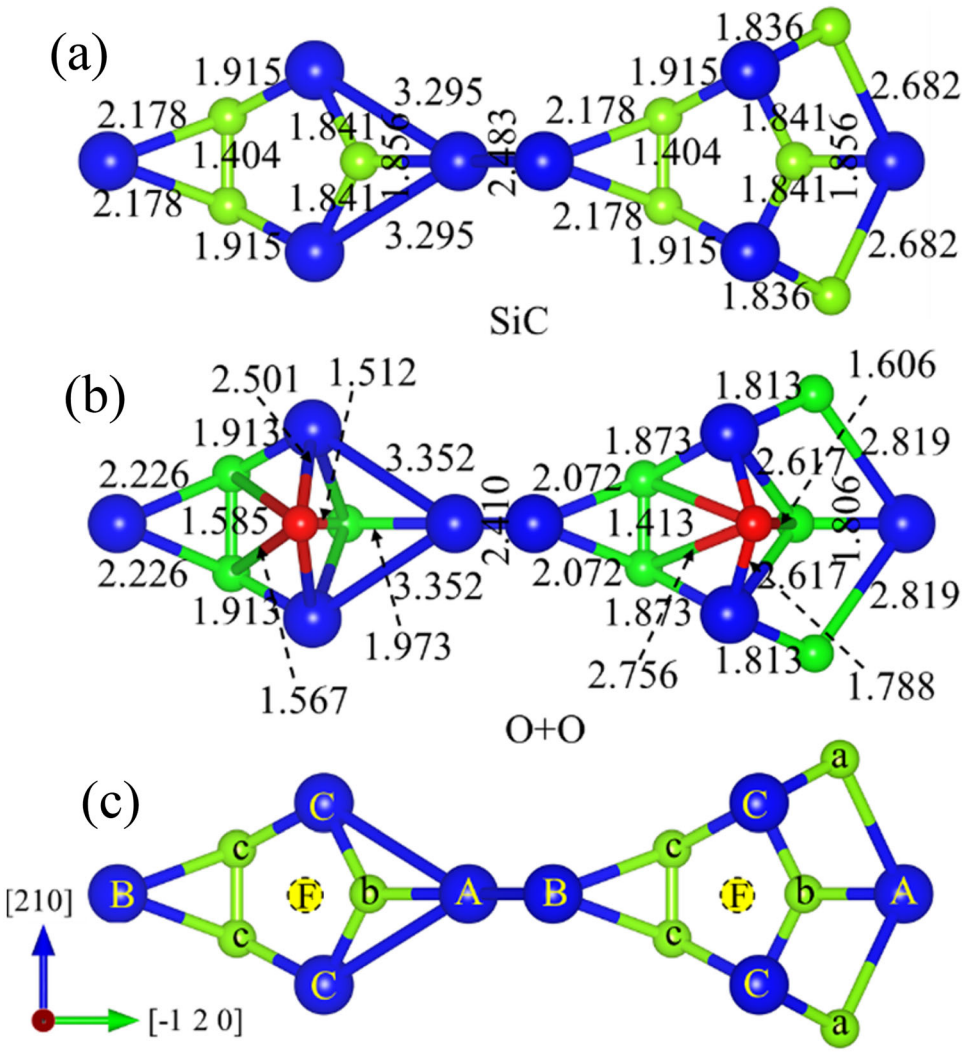

Fig. 22 (Color online) The diagram shows partial bond lengths (Å) on Σ5(210) GB with and without nonmetallic impurities. **a** Pure SiC, **b** O + O, **c** Numbering of atomic sites

impurities were explored to determine the underlying electronic interactions in the bonding.

Finally, the conclusions of the co-segregation investigation suggest that high concentrations of Bi and Pb result in the consumption of O at the Σ5(210) GBs, whereas low concentrations of Bi and Pb result in an enrichment of O at these GBs. An increase in temperature also inhibits the consumption of O by Bi and Pb. In addition, the bonding of Pb or Bi is not strongly influenced by other impurities at the Σ5(210) GBs.

In summary, a comprehensive investigation was conducted in this research on the structure and energy of the Σ5(210) GBs of doped SiC from the atomic and electronic perspectives. The current results may be valuable for the development of new ceramics with high corrosion resistance.

Author contributions All authors contributed to the study conception and design. Material preparation, data collection and analysis were performed by Jun Hui, Wen-Guan Liu, Bao-Liang Zhang, Tao Liu, and Min Liu. The first draft of the manuscript was written by Jun Hui and Wen-Guan Liu, and all authors commented on previous versions of the manuscript. All authors read and approved the final manuscript.

References

1. X. Shi, B. Li, H. Liu et al., The corrosion resistance mechanisms of the Cr-coated SiC in molten Na_2SO_4 salt: strengthened boundaries and protective scales. Corros. Sci. **185**, 109421 (2021). https://doi.org/10.1016/j.corsci.2021.109421
2. S.L. Chen, X.J. He, C.X. Yuan et al., Recent studies on potential accident-tolerant fuel-cladding systems in light water reactors. Nucl. Sci. Tech. **31**, 32 (2020). https://doi.org/10.1007/s41365-020-0741-9
3. C. Cluzel, E. Baranger, P. Ladevèze et al., Mechanical behavior and lifetime modelling of self-healing ceramic-matrix composites subjected to thermo-mechanical loading in air. Composites A **40**, 976–984 (2009). https://doi.org/10.1016/j.compositesa.2008.10.020

4. Z.X. Tan, J.J. Cai, Neutronic analysis of silicon carbide cladding accident-tolerant fuel assemblies in pressurized water reactors. Nucl. Sci. Tech. **30**, 48 (2019). https://doi.org/10.1007/s41365-019-0575-5
5. S. Kondo, M. Lee, T. Hinoki et al., Effect of irradiation damage on hydrothermal corrosion of SiC. J. Nucl. Mater. **464**, 36–42 (2015). https://doi.org/10.1016/j.jnucmat.2015.04.034
6. B. Wang, C. Zhang, X. Ma et al., Key problems on the mechanical behavior of nuclear materials and structures of pressured water reactors. Sci. Sin. Phys. Mech. Astron. **49**, 114602 (2019). https://doi.org/10.1360/SSPMA-2019-0113
7. S. Kondo, S. Mouri, Y. Hyodo et al., Role of irradiation-induced defects on SiC dissolution in hot water. Corros. Sci. **112**, 402–407 (2016). https://doi.org/10.1016/j.corsci.2016.08.007
8. S. Kondo, K. Seki, Y. Maeda et al., Contribution of dangling-bonds to polycrystalline SiC corrosion. Scr. Mater. **188**, 6–9 (2020). https://doi.org/10.1016/j.scriptamat.2020.07.001
9. C.M. Parish, K.A. Terrani, Y.J. Kim et al., Microstructure and hydrothermal corrosion behavior of NITE-SiC with various sintering additives in LWR coolant environments. J. Eur. Ceram. Soc. **37**, 1261–1279 (2017). https://doi.org/10.1016/j.jeurceramsoc.2016.11.033
10. P.J. Doyle, S. Zinkle, S.S. Raiman, Hydrothermal corrosion behavior of CVD SiC in high temperature water. J. Nucl. Mater. **539**, 152241 (2020). https://doi.org/10.1016/j.jnucmat.2020.152241
11. S. Özkan, G. Hapç, G. Orhan et al., Electrodeposited Ni/SiC nanocomposite coatings and evaluation of wear and corrosion properties. Surf. Coat. Technol. **232**, 734–741 (2013). https://doi.org/10.1016/j.surfcoat.2013.06.089
12. V. Zarghami, M. Ghorbani, Alteration of corrosion and nano mechanical properties of pulse electrodeposited Ni/SiC nanocomposite coatings. J. Alloys Compd. **598**, 236–242 (2014). https://doi.org/10.1016/j.jallcom.2014.01.220
13. T.M. Kondo, M. Kondo, Corrosion resistance of ceramics SiC and Si_3N_4 in flowing lead-bismuth eutectic. Prog. Nucl. Energy **53**, 1061–1065 (2011). https://doi.org/10.1016/j.pnucene.2011.04.023
14. L.Y. He, G.C. Li, S.P. Xia et al., Effect of 37Cl enrichment on neutrons in a molten chloride salt fast reactor. Nucl. Sci. Tech. **31**, 27 (2020). https://doi.org/10.1007/s41365-020-0740-x
15. R. Tu, Q. Liu, Y. Li et al., First principles calculations for iodine atom diffusion in SiC with point defects. Comput. Mater. Sci. **142**, 427–436 (2018). https://doi.org/10.1016/j.commatsci.2017.10.025
16. D. Shrader, L. Szlufarska, D. Morgan, Cs diffusion in cubic silicon carbide. J. Nucl. Mater. **421**, 89–96 (2012). https://doi.org/10.1016/j.jnucmat.2011.11.051
17. D. Shrader, S.M. Khalil, T. Gerczak et al., Ag diffusion in cubic silicon carbide. J. Nucl. Mater. **408**, 257–271 (2011). https://doi.org/10.1016/j.jnucmat.2010.10.088
18. P.F. Zhang, Y.L. Zhang, W. Gai et al., Oxidation behaviour of SiC ceramic coating for C/C composites prepared by pressureless reactive sintering in wet oxygen: Experiment and first-principle simulation. Ceram. Int. **47**, 15337–15348 (2021). https://doi.org/10.1016/j.ceramint.2021.02.099
19. P. Qing, N.J. Chen, W.F. Skerjanc et al., Reveal the fast and charge-insensitive lattice diffusion of silver in cubic silicon carbide via first-principles calculations. Comput. Mater. Sci. **170**, 109190 (2019). https://doi.org/10.1016/j.commatsci.2019.109190
20. T.M. Lillo, I.J. Rooyen, Influence of SiC GB character on fission product transport in irradiated TRISO fuel. J. Nucl. Mater. **473**, 83–92 (2016). https://doi.org/10.1016/j.jnucmat.2016.01.040
21. A. Lara, A. Muñoz, M. Castillo-Rodríguez et al., High-temperature compressive creep of spark-plasma sintered additive-free polycrystalline β-SiC. J. Eur. Ceram. Soc. **32**, 3445–3451 (2012). https://doi.org/10.1016/j.jeurceramsoc.2012.04.041
22. B. Wei, J. Zhou, Z. Yao et al., The effect of Ag nanoparticles content on dielectric and microwave absorption properties of β-SiC. Ceram. Int. **46**, 5788–5798 (2020). https://doi.org/10.1016/j.ceramint.2019.11.029
23. T. Koyanagi, Y. Katoh, T. Hinoki et al., Progress in development of SiC-based joints resistant to neutron irradiation. J. Eur. Ceram. Soc. **40**, 1023–1034 (2020). https://doi.org/10.1016/j.jeurceramsoc.2019.10.055
24. Z.F. Huang, F. Chen, Q. Shen et al., Combined effects of nonmetallic impurities and planned metallic dopants on GB energy and strength. Acta. Mater. **166**, 113–125 (2019). https://doi.org/10.1016/j.actamat.2018.12.031
25. Z.F. Huang, F. Chen, Q. Shen et al., Uncovering the influence of common nonmetallic impurities on the stability and strength of a Σ5 (310) GB in Cu. Acta. Mater. **148**, 110–122 (2018). https://doi.org/10.1016/j.actamat.2018.01.058
26. D. Scheiber, K. Prabitz, The influence of alloying on Zn liquid metal embrittlement in steels. Acta. Mater. **195**, 750–760 (2020). https://doi.org/10.1016/j.actamat.2020.06.001
27. M.H. Razmpoosh, C. DiGiovanni, Y.N. Zhou et al., Pathway to understand liquid metal embrittlement (LME) in Fe-Zn couple: From fundamentals toward application. Prog. Mater. Sci. **29**, 100798 (2021). https://doi.org/10.1016/j.pmatsci.2021.100798
28. H. Liang, X. Yao, J.X. Zhang et al., The effect of rare earth oxides on the pressureless liquid phase sintering of α-SiC. J. Euro. Ceram. Soc. **34**, 2865–2874 (2014). https://doi.org/10.1016/j.jeurceramsoc.2014.03.029
29. L. Tan, T.R. Allena, J.D. Hunn et al., EBSD for microstructure and property characterization of the SiC coating in TRISO fuel particles. J. Nucl. Mater. **372**, 400–404 (2008). https://doi.org/10.1016/j.jnucmat.2007.04.048
30. S. Xu, X. Li, Y. Zhao et al., Micromechanical properties and microstructural evolution of Amosic-3 SiC/SiC composites irradiated by silicon ions. J. Eur. Ceram. Soc. **8**, 2811–2820 (2020). https://doi.org/10.1016/j.jeurceramsoc.2020.02.023
31. B. Li, H. Liu, T. Shen et al., Irradiation induced microstructure damage in He-irradiated 3C-SiC at 1000. J. Eur. Ceram. Soc. **40**, 1014–1022 (2019). https://doi.org/10.1016/j.jeurceramsoc.2019.11.026
32. K. Jina, C. Lu, L.M. Wang et al., Effects of compositional complexity on the ion-irradiation induced swelling and hardening in Ni-containing equiatomic alloys. Scr. Mater. **119**, 65–70 (2016). https://doi.org/10.1016/j.scriptamat.2016.03.030
33. F.A. Garner, M.B. Toloczko, B.H. Sencer, Comparison of swelling and irradiation creep behavior of fcc-austenitic and bcc-ferritic/martensitic alloys at high neutron exposure. J. Nucl. Mater. **276**, 123–142 (2000). https://doi.org/10.1016/S0022-3115(99)00225-1
34. L.M. Wang, R.A. Dodd, G.L. Kulcinski et al., Effects of 14 MeV nickel ion irradiation on nickel-copper alloys observed in cross-section. J. Nucl. Mater. **155–157**, 1241–1248 (1988). https://doi.org/10.1016/0022-3115(88)90504-1
35. G. Chen, Y. Lei, Q. Zhu et al., Corrosion behavior of CLAM steel weld bead in flowing Pb-Bi at 550 °C. J. Nucl. Mater. **515**, 187–198 (2018). https://doi.org/10.1016/j.jnucmat.2018.12.038
36. P.G. Baranov, A.P. Bundakova, A.A. Soltamova et al., Silicon vacancy in SiC as a promising quantum system for single-defect and single-photon spectroscopy. Phys. Rev. B **83**, 125203 (2011). https://doi.org/10.1103/PhysRevB.83.125203
37. J.R. Weber, W.F. Koehl, J.B. Varley et al., Quantum computing with defects. Proc. Natl. Acad. Sci. USA **107**, 8513–8518 (2010). https://doi.org/10.1073/pnas.1003052107

38. E.P. Loewen, A.T. Tokuhiro, Status of research and development of the lead alloy cooled fast reactor. J. Nucl. Sci. Technol. **40**, 614–627 (2003). https://doi.org/10.1080/18811248.2003.9715398
39. B.S. Lou, C.A. Yen, Y. Chen et al., Effects of processing parameters on the adhesion and corrosion resistance of oxide coatings grown by plasma electrolytic oxidation on AZ31 magnesium alloys. J. Mater. Sci. Technol. **10**, 1355–1371 (2021). https://doi.org/10.1016/j.jmrt.2020.12.108
40. L. Lin, Y. Chen, L. Hua et al., Electronic structures and ferromagnetism of 3C-SiC doped with (Fe, Co) double-impurities by first-principles calculations. Mater. Sci. Semicon. Proc. **129**, 105779 (2021). https://doi.org/10.1016/j.mssp.2021.105779
41. P. Zhang, Y. Zhang, Initial oxidation of 3C-SiC (111) in oxidizing atmosphere containing water vapor: H_2O adsorption from first-principles calculation. Mater. Today. Commun. **26**, 102072 (2021). https://doi.org/10.1016/j.mtcomm.2021.102072
42. B. Li, H. Liu, T. Shen et al., Irradiation-induced microstructure damage in He-irradiated 3C-SiC at 1000°C. J. Eur. Ceram. Soc. **40**, 1014–1022 (2019). https://doi.org/10.1016/j.jeurceramsoc.2019.11.026
43. J. Hui, W. Liu, B. Wang, Theoretical study of the effects of alloying elements on Cu nanotwins. Sci. China-Phys. Mech. Astron. **63**, 104612 (2020)
44. J. Hui, X.Y. Zhang, W. Liu et al., First-principles study of detwinning in a FCC alloy. J. Sol. State Chem. **293**, 121765 (2021). https://doi.org/10.1016/j.jssc.2020.121765
45. G. Kresse, J. Furthmuller, Efficient iterative schemes for ab initio total-energy calculations using a plane-wave basis set. Phys. Rev. B. **54**, 11169–11186 (1996)
46. W. Kohn, L.J. Sham, Self-consistent equations including exchange and correlation effects. Phys. Rev. B. **140**, A1133 (1965)
47. P.E. Blöchl, Projector augmented-wave method. Phys. Rev. B **50**, 17953–17979 (1994)
48. W. Gordy, W.J.O. Thomas, Electronegativities of the elements. J. Chem. Phys. **24**, 439–444 (1956). https://doi.org/10.1063/1.1742493
49. T.W. Fan, Z.P. Wang, J.J. Lin et al., First-principles predictions for stabilizations of multilayer nanotwins in Al alloys at finite temperatures. J. Alloys Compd. **783**, 765–771 (2019). https://doi.org/10.1016/j.jallcom.2018.12.314
50. A. Kumar, J. Wang, C.N. Tomé et al., First-principles study of energy and atomic solubility of twinning-associated boundaries in hexagonal metals. Acta. Mater. **85**, 144–154 (2015). https://doi.org/10.1016/j.actamat.2014.11.015
51. Q.Y. Wang, C. Wang, Molecular dynamics analysis of the thermal conductivity of SiC grain boundaries under irradiation conditions. J. Mater. Sci. Eng. **34**, 133–136 (2016). https://doi.org/10.14136/j.cnki.issn1673-2812.2016.01.025
52. S. Dinda, W.R. Warke, The effect of grain boundary segregation on liquid metal induced embrittlement of steel. Mater. Sci. Eng. **24**, 199–208 (1976). https://doi.org/10.1016/0025-5416(76)90113-0
53. M. Vsianska, M. Šob, The effect of segregated sp-impurities on grain-boundary and surface structure, magnetism and embrittlement in nickel. Prog. Mater. Sci. **56**, 817–840 (2011). https://doi.org/10.1016/j.pmatsci.2011.01.008
54. C. He, Z. Li, H. Chen et al., Unusual solute segregation phenomenon in coherent twin boundaries. Nat. Commun. **12**, 722 (2021). https://doi.org/10.1038/s41467-021-21104-8
55. X.J. Zhao, H.W. Chen, N. Wilson et al., Direct observation and impact of cosegregated atoms in magnesium having multiple alloying elements. Nat. Commun. **10**, 3243 (2019)
56. Y.M. Zhu, S.W. Xu, J.F. Nie et al., 1011 Twin boundary structures in a Mg–Gd alloy. Acta Mater **143**, 1–12 (2018). https://doi.org/10.1016/j.actamat.2017.09.067
57. H. Zhou, G.M. Cheng, X.L. Ma et al., Effect of Ag on interfacial segregation in MgGdYAgZr alloy. Acta Mater. **95**, 20–29 (2015). https://doi.org/10.1016/j.actamat.2015.05.020
58. X.F. Chen, L.R. Xiao, Z.G. Ding et al., Atomic segregation at twin boundaries in a MgAg alloy. Scr. Mater. **178**, 193–197 (2020). https://doi.org/10.1016/j.scriptamat.2019.11.025
59. L. Pauling, Atomic radii and interatomic distances in metals. J. Am. Chem. Soc. **69**, 542–553 (1947)
60. A.M. Kueck, D.J. He, Two-stage sintering inhibits abnormal grain growth during beta to alpha transformation in SiC. J. Eur. Ceram. Soc. **28**, 2259–2264 (2008). https://doi.org/10.1016/j.jeurceramsoc.2008.01.026
61. Q.Q. Shao, L.H. Liu, T.W. Fan et al., Effects of solute concentration on the stacking fault energy in copper alloys at finite temperatures. J. Alloys Compd. **726**, 601–607 (2017). https://doi.org/10.1016/j.jallcom.2017.07.332
62. L. Huber, J. Rottler, M. Militzer, Atomistic simulations of the interaction of alloying elements with grain boundaries in Mg. Acta Mater. **80**, 194–204 (2014). https://doi.org/10.1016/j.actamat.2014.07.047
63. P. Garg, I. Adlakha, K.N. Solanki, Effect of solutes on ideal shear resistance and electronic properties of magnesium: a first-principles study. Acta. Mater. **153**, 327–335 (2018). https://doi.org/10.1016/j.actamat.2018.05.014
64. C.L. White, W.A. Coghlan, The spectrum of binding energies approach to GB segregation. Metall. Trans. A **8**, 1403–1412 (1977)
65. J. Hui, W. Liu, B. Wang, Quasi-gradient variation of microstructures and properties of Cu–Sn alloy along the thickness direction under cold spinning. J. Alloys Compd. **831**, 154701 (2020). https://doi.org/10.1016/j.jallcom.2020.154701
66. R. Janisch, C. Elsässer, Segregated light elements at grain boundaries in niobium and molybdenum. Phys. Rev. B. **67**, 2209–2219 (2003)
67. C.T. Ser, A.M. Mak, T. Wejrzanowski et al., Designing piezoresistive materials from first-principles: dopant effects on 3C-SiC. Comp. Mater. Sci. **186**, 110040 (2021). https://doi.org/10.1016/j.commatsci.2020.110040
68. M. Luo, Y.E. Xu, Y.X. Song et al., Impact of isotropic strain on electronic and magnetic properties of O-adsorbed SiC monolayer. Mater. Sci. Semicond. Process. **83**, 27–32 (2018). https://doi.org/10.1016/j.mssp.2018.04.005
69. P. Lejcek, Grain boundary segregation in metals. Springer Ser. Mater. Sci. **136**, 1–239 (2010). https://doi.org/10.1007/978-3-642-12505-8
70. D. Scheiber, L. Romaner, R. Pippan et al., Impact of solute-solute interactions on grain boundary segregation and cohesion in molybdenum. Phys. Rev. Mater. **2**, 93609 (2018)
71. J. Hui, G. Yang, M. Liu et al., Effects of alloy compositions on hydrogen behaviors at a nickel grain boundary and a coherent twin boundary. Inter. J. Hydr. Energy **45**, 10951–10961 (2020). https://doi.org/10.1016/j.ijhydene.2020.02.008
72. G.C. Li, Z. Yang, C.G. Yu et al., Influences of ^{7}Li enrichment on Th-U fuel breeding for an improved molten salt fast reactor (IMSFR). Nucl. Sci. Technol. **28**, 97 (2017). https://doi.org/10.1007/s41365-017-0250-7